Check for updates

OPEN

Mass-sensitive particle tracking to elucidate the membrane-associated MinDE reaction cycle

Tamara Heermann [1,5], Frederik Steiert [1,2,5], Beatrice Ramm [1,3], Nikolas Hundt [4,5 ✉] and Petra Schwille [1 ✉]

In spite of their great importance in biology, methods providing access to spontaneous molecular interactions with and on biological membranes have been sparse. The recent advent of mass photometry to quantify mass distributions of unlabeled biomolecules landing on surfaces raised hopes that this approach could be transferred to membranes. Here, by introducing a new interferometric scattering (iSCAT) image processing and analysis strategy adapted to diffusing particles, we enable mass-sensitive particle tracking (MSPT) of single unlabeled biomolecules on a supported lipid bilayer. We applied this approach to the highly nonlinear reaction cycles underlying MinDE protein self-organization. MSPT allowed us to determine the stoichiometry and turnover of individual membrane-bound MinD/MinDE protein complexes and to quantify their size-dependent diffusion. This study demonstrates the potential of MSPT to enhance our quantitative understanding of membrane-associated biological systems.

The recruitment of proteins to lipid interfaces is crucial for various cell biological processes, such as the regulation of membrane trafficking[1], mediation of signaling cascades[2] and the establishment of cell polarity. These membrane-associated reactions often rely on short-lived complexes that coexist in a dynamic equilibrium with their respective cytosolic forms[3]. Transient interactions on the membrane eventually serve as nucleation sites for the assembly of larger, more stable complexes. Additionally, the spatial distribution, stoichiometry and temporal dynamics of membrane-associated complexes are often heterogeneous[4]. This combination of fast dynamics and compositional heterogeneity makes membrane-associated reactions difficult targets for conventional analytical techniques, which determine the composition and follow the dynamics of molecular systems based on ensemble-averaged measures[5]. In recent decades, single-particle tracking (SPT) has revolutionized the analysis of membrane-associated systems by following the dynamics of individual molecules at nanometer precision and millisecond time resolution[6–8], using fluorophores as labels in combination with highly sensitive microscopy. More recently, scattering-based detection using gold nanoparticles as labels has pushed the spatiotemporal resolution down to the subnanometer and microsecond range[9–12]. The single-molecule nature of these approaches has provided detailed mechanistic insight into the dynamics of biomolecular systems[13]. However, as a label-based technique, SPT also suffers from label-induced artifacts: large particles, but also small fluorescent tags[14] may perturb native protein function, and fluorescence-specific phenomena such as photobleaching and -blinking hinder continuous particle tracking and limit the attainable spatiotemporal resolution[15]. More importantly, although fluorescence-based SPT may provide access to interaction dynamics between tagged molecules through brightness changes, it has proved extremely complicated to extract the molecular composition of the tracked particles. In general, relating the signal of an external marker to the molecular

stoichiometry of the labeled particle requires careful characterization of labeling efficiencies and imaging conditions, which is very often hampered by quenching effects. Especially for multicomponent systems, access to the molecular composition of single particles has been prohibitive for standard biological applications.

Recent advances in interferometric scattering (iSCAT) microscopy[11,16] made it possible to detect individual biomolecules label-free based on light scattering. The linear relationship between iSCAT contrast and molecular mass of a biomolecule led to the development of mass photometry[17,18]. This technique allows the determination of size distributions of biomolecules in solution by measuring the individual masses of molecules landing on a glass surface and counting their relative abundances to determine both molecular identity and composition. For purely shot noise-limited detection of a single molecule landing on a glass surface on top of the static scattering pattern, mass photometry applies a sophisticated background removal strategy optimized for this type of experiment, which is not compatible with the detection of mobile molecules diffusing on lipid membranes. Here, by introducing a new iSCAT image processing and analysis strategy, we enable mass-sensitive particle tracking (MSPT) of single unlabeled biomolecules on a supported lipid bilayer (SLB). We show that the iSCAT signal-to-mass linearity holds true for membrane-associated proteins and that we can relate molecular composition, accessible via mass, to diffusive behavior. Moreover, we can follow the mass time course along individual trajectories, making it possible to observe the (dis-)assembly of biomolecular complexes in real-time. The approach is fast and provides high particle statistics within minutes, all without need for protein labeling and its caveats.

We showcase the abilities of this method for the detailed analysis of complex biological systems by analyzing the membrane-associated reaction cycle of the *Escherichia coli* Min system. This system consists of three proteins—MinC, MinD and MinE—and is essential for the spatiotemporal regulation of the

[1]Department of Cellular and Molecular Biophysics, Max Planck Institute of Biochemistry, Planegg, Germany. [2]Department of Physics, Technical University Munich, Garching, Germany. [3]Department of Physics, Princeton University, Princeton, NJ, USA. [4]Department of Cellular Physiology, Biomedical Center (BMC), Ludwig-Maximilians-Universität München, Planegg, Germany. [5]These authors contributed equally: Tamara Heermann, Frederik Steiert, Nikolas Hundt. ✉e-mail: nikolas.hundt@med.uni-muenchen.de; schwille@biochem.mpg.de

division site in *E. coli*[19]. To perform this task, the ATPase MinD and the ATPase-activating protein MinE oscillate between the cell poles, forming a concentration gradient of the passenger protein MinC. This gradient supposedly enables MinC to inhibit FtsZ protein polymerization at the poles and directs Z-ring formation to the mid-cell[20,21]. To this end, the phospholipid bilayer acts as a catalytic interface and membrane interaction of MinD and MinE is mediated by amphipathic helices, that is membrane targeting sequences (MTS)[22–25]. The interaction of MinD and MinE with the membrane decreases their diffusion rates and facilitates lateral molecular interactions enabling the system to self-organize[26]. Despite its compositional simplicity, the system exhibits complex, nonlinear dynamics. Its self-organization can be reconstituted in vitro[26] and the underlying mechanism has been probed by various techniques such as SPT[13], high-speed atomic force microscopy[27], nuclear-magnetic resonance[28], electron microscopy[29], plasmonic nanosensors[30] and mutational analysis[31,32]. Despite this intense characterization, molecular details about MinDE self-assembly, such as the presumed cooperativity in bilayer-attachment of MinD, have remained poorly understood. Thus, the system was set to benefit from the unique ability of MSPT to characterize dynamics as well as molecular composition of membrane-attached protein complexes. Using MSPT, we dissected the membrane-associated MinDE reaction cycle by determining the stoichiometry, turnover and diffusion of individual membrane-bound MinD/MinDE protein complexes. Our results indicate that MinD, in contrast to the classical model, assembles not only into dimers, but also forms larger oligomers, confirming recent findings[27]. We furthermore show that MinE promotes MinD self-assembly on the lipid bilayer due to its ability to interconnect MinD into so far unresolved higher-order heteromeric complexes. We believe our experiments on the Min system demonstrate that MSPT is a powerful, widely applicable tool for the mechanistic analysis of both pro- and eukaryotic membrane-associated systems.

Results

Dynamic mass-imaging of membrane-associated protein complexes. The major obstacle for detecting single macromolecules with iSCAT microscopy (Fig. 1a) is separating their comparatively small signal from the dominant scattering background. In a standard mass photometry experiment, molecules landing on a glass surface are detected through continuous comparison of an averaged image with the average of its preceding frames as background (Supplementary Fig. 1a)[17,18]. In this image processing approach, a molecule appears as a dark spot at the moment of landing and disappears when it becomes part of the static background[17]. The mass of the particle can then be determined by fitting the detected peak signal with a model point spread function (PSF). However, for a moving molecule, this strategy produces distorted images of the molecule's PSF. The missing particle density at its previous location produces a bright spot, while the added density at the new position generates a dark spot. The spatial overlap of these patterns causes moving objects to appear as dark fronts carrying bright tails, thus hampering the determination of their mass and location (Supplementary Fig. 1b and Supplementary Video 1). To address this issue, we used the temporal median of an image sequence as background estimate[10,33,34]. If during the median period moving molecules only occasionally cross a surface location, the median signal at that location will be a good estimate of the empty background. To retain shot noise-limited detection, which is strongly affected by sample drift, we calculated the pixel-wise median of an image sequence as background estimate for its central frame and moved this median window from frame to frame throughout the video (Supplementary Fig. 1c). Due to the clear separation of static background from moving objects, background-corrected videos showed clear, undistorted images of moving PSFs (Fig. 1a, Supplementary Fig. 1c, Supplementary Table 1 and Supplementary

Video 1), a prerequisite that allows MSPT of single unlabeled biomolecules diffusing on lipid interfaces.

First, we set out to assess the quality of mass determination of mobile molecules compared to landing particles in conventional mass photometry. To this end, we used a bilayer supplemented with biotinylated lipids and attached a set of biotinylated standard proteins with known mass via divalent streptavidin[35]. This system has several advantages, such as the ability to cover different protein size regimes, standardized membrane binding and the added benefit of simplified complex stoichiometries by using divalent streptavidin. For each molecule, we determined its median contrast throughout its trajectory. Analogous to conventional mass photometry (Fig. 1b, left column), histograms of the contrasts of all molecules determined with MSPT revealed the particle size distribution (Fig. 1b, right column and Supplementary Video 2). For our standard proteins, iSCAT contrast as a function of mass exhibited the expected linear relationship[17]. The calibration line obtained from standards diffusing on SLBs was in fact indistinguishable from the one determined with molecules landing on glass (Fig. 1c). This result indicates that mass calibrations performed with landing assays can be transferred to particles diffusing on membranes. However, this strictly needs to be verified for any new lipid/buffer combination, protein system and imaging condition.

Besides mass determination, MSPT also enables the analysis of the diffusive behavior of membrane-bound molecules. For this purpose, it is important to choose the median window size for background estimation such that particles travel sufficient distances during the median period. Hence, we first systematically tested the minimum median window sizes required to extract the correct diffusion coefficients at particle diffusion speeds expected for our SLB system. We generated artificial videos of randomly diffusing particles at varying speeds and compared the input diffusion coefficients with diffusion coefficients extracted using different median window sizes and extraction methods (see Methods, Supplementary Figs. 2 and 3 as well as Supplementary Discussion for details). Based on the results of our simulation, we chose a jump-distance distribution analysis[36] to extract diffusion coefficients from our experimental videos. As an experimental verification of the diffusion coefficients obtained in this manner, we again made use of streptavidin attached to a membrane via biotinylated lipids. In line with literature values ranging from 0.8 to 2.0 $\mu m^2 s^{-1}$ (refs. [37–39]), the lateral diffusion coefficient of streptavidin was found to be $1.3 \pm 0.1 \mu m^2 s^{-1}$ (Fig. 1d). Similar diffusion coefficients were obtained for all standard proteins attached via divalent streptavidin (Supplementary Fig. 4). To highlight a unique advantage of MSPT, we plotted the diffusion coefficient versus the respective molecular mass obtained from individual trajectories, enabling an unprecedented direct connection of these two parameters. As displayed in Fig. 1d, the unimodal distribution of membrane-bound streptavidin indicates a distinct population of tetramers undergoing Brownian motion. Having validated the method with membrane-attached streptavidin, we thought the method offers the potential of detailed insight into the dynamics of molecular interactions within more complex membrane-bound systems. To further explore the method's capabilities, we turned to the membrane-associated *E. coli* Min system.

Cooperative membrane-catalyzed association dynamics of MinD. The MinDE system is known for its ability to self-organize into mesoscopic protein patterns on lipid membranes[26]. To generate these patterns, MinD and MinE are generally assumed to undergo a canonical membrane binding–unbinding cycle displayed in Fig. 2a. In brief, on ATP complexation, cytosolic MinD dimerizes and localizes to the membrane interface[23]. After homodimeric MinE binds to MinD, nucleotide hydrolysis is stimulated and MinD dissociates from the lipid bilayer to return to its monomeric state[40]. Despite this established model, it has remained rather enigmatic how
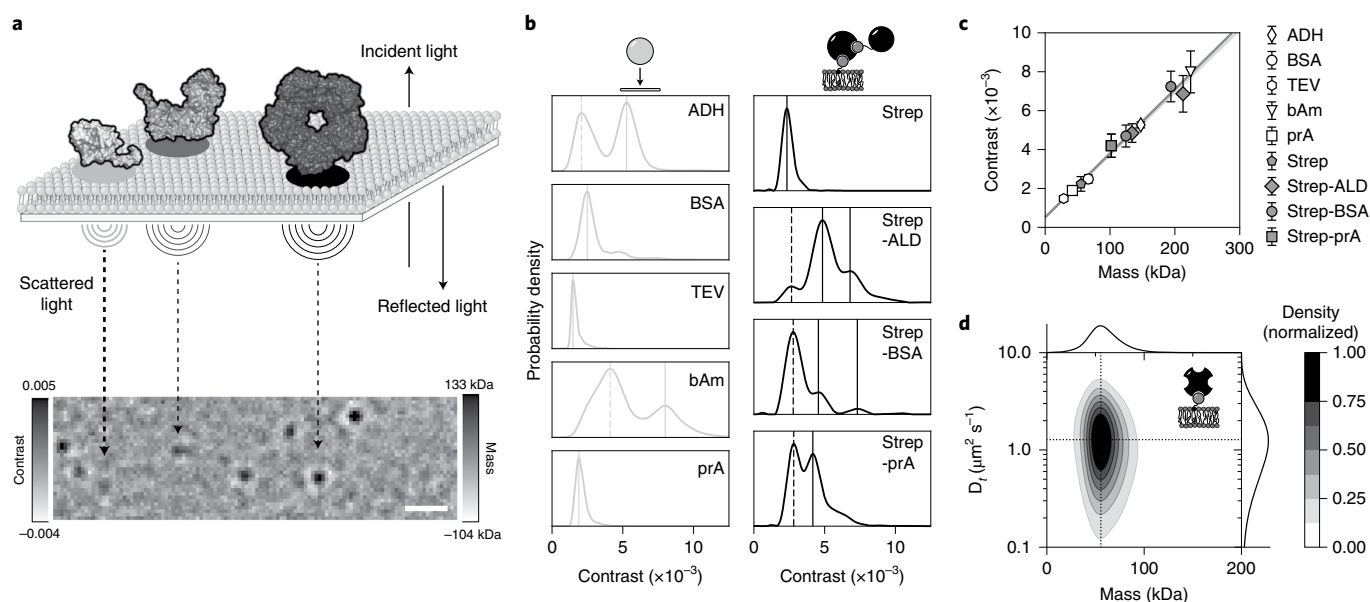
Fig. 1 | Principle of MSPT. a, Schematic displaying the iSCAT-based measurement principle of MSPT. Exemplary structures of three aldolase oligomer states (PDB 4S1F, ref. [51]) are shown in the top panel, and their respective iSCAT images at the bottom. Scale bar, 1 μm. **b**, Probability density distributions of standard proteins determined using the conventional mass photometry landing assay (left) or using MSPT (right). All data represent pooled distributions of three independent experiments per condition: alcohol dehydrogenase (ADH) (particle number $n = 9,828$), BSA ($n = 11,408$), TEV protease (TEV) ($n = 1,705$), β-amylase (bAm) ($n = 10,043$), protein A (prA) ($n = 12,720$); divalent streptavidin (Strep) ($n = 16,699$ trajectories), divalent streptavidin with biotinylated aldolase (Strep-ALD) ($n = 16,727$ trajectories), divalent streptavidin with biotinylated BSA (Strep-BSA) ($n = 8,842$ trajectories) and divalent streptavidin with biotinylated protein A (Strep-prA) ($n = 22,424$ trajectories). Dashed lines mark peaks not considered for mass calibration (left). Continuous lines represent oligomer states included in the mass calibration. Two-dimensional plots of mass versus diffusion coefficient for the four proteins measured with MSPT (right) are shown in Supplementary Fig. 4. **c**, Comparison of the contrast-to-mass calibration for mass photometry and MSPT, derived from peak contrasts in **b** and their assigned sequence masses (Supplementary Tables 2 and 3). Error bars represent the standard error of the peak locations estimated by bootstrapping. **d**, Two-dimensional KDE of 1.25 nM tetravalent streptavidin bound to biotinylated lipids on a SLB ($n = 73,901$ trajectories of three independent replicates; particle density: 0.2 μm^{-2}). Marginal probability distributions of the molecular mass (top) and the diffusion coefficient (right) are presented.

ATP-dependent dimerization and the resulting increase in MinD membrane affinity alone can confer the nonlinear attachment required for pattern formation. In recent years, it has been proposed that the presence of higher MTS valences and thus higher-order oligomer structures might contribute to the local self-enhancement of MinD at the membrane[27,31,41]. Due to the fast diffusion and attachment or detachment dynamics, however, it has remained challenging to provide convincing evidence of their existence.

Taking advantage of the ability to monitor the mass of membrane-attached and diffusing protein complexes, we thus applied our MSPT approach to investigate potential oligomeric species formed by the MinDE system. We started by reconstituting the membrane recruitment of MinD and compared the mass distribution of MinD in solution, measured in a mass photometry landing assay, with the mass distribution of MinD on a lipid bilayer (Fig. 2b and Supplementary Fig. 5). In the presence of ATP, MinD monomers were detected as the predominant species in solution. In contrast, the main species on the membrane was a MinD dimer already at sparse densities corresponding to one particle per frame in the field of view (31.9 μm²). However, it should be noted that at the chosen imaging conditions for MSPT, the signal-to-noise ratio of monomers (33 kDa) was too low for their quantitative detection (Supplementary Figs. 9 and 10). Hence, an adequate estimate of their membrane abundance cannot be stated.

One of the main advantages of iSCAT-based imaging is that it provides a direct estimate of the molecular density on a bilayer from the number of detected particles, compared to single-molecule fluorescence where factors such as labeling efficiency and photobleaching have to be taken into account. Accordingly, we could classify

video sections of membrane-bound MinD into conditions of different particle densities and observed the resulting change in the oligomeric distribution (Fig. 2c, Supplementary Figs. 6 and 7 and Supplementary Video 3). While MinD was mainly present in the dimer state at low particle densities (0.1 μm^{-2}), the MinD population shifted toward a broad distribution with higher-order complexes on crowded bilayers (0.8 μm^{-2}). These data directly demonstrate that MinD indeed assembles into complexes larger than a dimer as previously suggested[27,31]. To further investigate the structural determinants for higher-order MinD assemblies, we performed the same MSPT experiment with a MinD mutant (D40A) that is reported to predominantly reside in the dimeric state due to its impaired ability to hydrolyze ATP[42]. According to the prevailing mechanism, it should not be possible for a locked dimer mutant to participate in MinD self-assembly, due to its inability to switch between the monomeric and dimeric state[23,40,43]. Nevertheless, we found a distinct population of MinD D40A tetramers in our contour plot (Fig. 2d and Supplementary Fig. 8), suggesting that MinD is capable of forming higher-order oligomers using an interface distinct from the canonical dimerization site.

Another aspect of the D40A mutant was its clear separation into two distinct populations (dimer and tetramer), whereas the distribution of the wild type (WT) protein appeared unresolved. This result indicates that the WT was able to also recruit MinD monomers forming trimeric species as intermediates, which were not as abundant for the D40A mutant. To provide a more quantitative measure for the comparison between WT and D40A mutant, we deconvolved their mass distributions into the underlying components to determine the relative abundance of each species as a
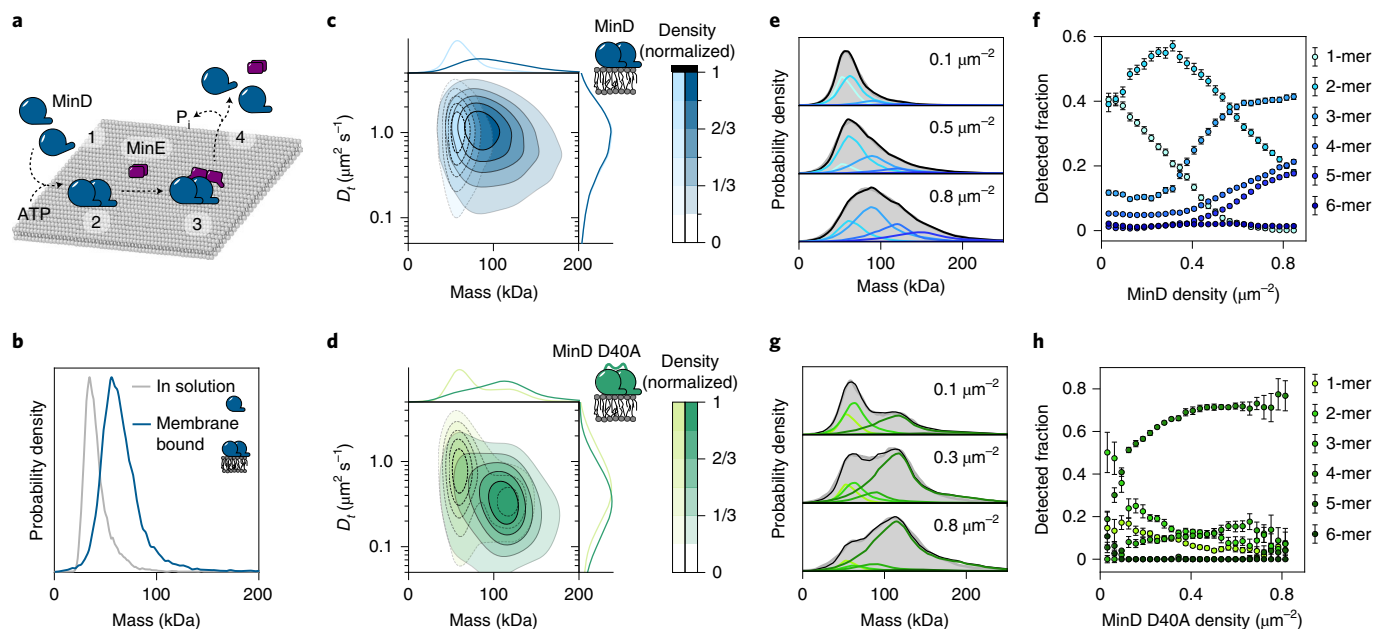
Fig. 2 | Lateral MinD–MinD interactions lead to self-assembly into large homo-oligomers. a, Schematic of the canonical membrane binding–unbinding cycle of MinDE. Upon ATP complexation, MinD dimerizes (1) and attaches to the membrane interface (2). In the event of MinE binding (3), MinE stimulates the intrinsic ability of MinD to hydrolyze ATP, which upon inorganic phosphate (P_i) release leads to the dissociation of MinD from the membrane in its monomeric form (4). **b**, MinD mass distribution in solution (gray line) ($n = 16,101$ particles) and on attachment to the SLB (blue line) ($n = 13,917$ trajectories). For solution experiments, 175 nM MinD with 0.5 µM ATP were measured in the conventional mass photometry landing assay. The membrane mass distribution of MinD was determined using MSPT at a particle density of 0.03 µm^{-2}. **c,d**, Two-dimensional KDE of membrane-attached MinD (**c**) and MinD D40A (**d**) at particle densities of 0.1 µm^{-2} (light blue) ($n = 117,086$ trajectories) and 0.8 µm^{-2} (dark blue) ($n = 152,685$ trajectories) and 0.1 µm^{-2} (light green) ($n = 7,831$ trajectories) and 0.8 µm^{-2} (dark green) ($n = 3,150$ trajectories), respectively. Marginal probability distributions of both molecular mass (top) and diffusion coefficient (right) are presented. **e,g**, Representative mass distributions (gray) of MinD (**e**) and MinD D40A (**g**) and estimation (black line, colored lines highlight underlying components) of its six components (MinD monomer–hexamer, light blue–dark blue; MinD D40A monomer–hexamer, light green–dark green) for three different particle densities (0.1 µm^{-2}, 0.3/0.5 µm^{-2} and 0.8 µm^{-2}). **f,h**, Relative oligomer abundance as a function of particle density: MinD (**f**) and MinD D40A (**h**). Error bars are the standard deviation of fitting results from three data subsets. The oligomer analysis is based on a total of $n = 1,102,940$ trajectories for MinD and $n = 194,545$ for MinD D40A.

function of particle density on the bilayer. To estimate the shapes of the individual components, we used our video simulation routine and determined separate mass distributions for particles representing only one type of MinD oligomer at a range of particle densities (Supplementary Figs. 9 and 10 and Supplementary Discussion). Next, we fit the mass distributions of MinD WT and D40A using a linear combination of simulated distributions from six components corresponding to monomers–hexamers and extracted the relative abundance of each oligomer as a function of particle density (Fig. 2e,g and Supplementary Fig. 11). These graphs show a sequential appearance of increasingly larger oligomers of MinD for higher molecule densities (Fig. 2f). Compared to the WT, the D40A mutant had a higher tendency to populate stoichiometries with even numbers of subunits and to transform its dimer state into the tetramer state, likely due to the increased stability of the dimer (Fig. 2h).

Furthermore, MSPT confers the unique possibility to determine oligomer-specific lateral diffusion coefficients. This knowledge can be used to deduce structural information about the observed molecules when considering the theory of Evans and Sackmann[44], which postulates the relation of an object's membrane inclusion size with its respective diffusion coefficient. Assuming a similar membrane viscosity as for pure dioleoyl-*sn*-glycero-3-phosphocholine (DOPC) membranes[45], we can thus estimate that a MinD D40A dimer with a diffusion coefficient of 0.85 µm^2 s^{-1} has an inclusion size of 5 nm, and a tetramer with 0.34 µm^2 s^{-1} an inclusion size of 9 nm (Supplementary Fig. 13). These estimates indicate that all monomers[42] of the tetramer are able to insert their

MTS into the bilayer, suggesting certain geometrical constraints for subunit orientation.

Time-resolved mass analysis of single MinD trajectories. Aside from measuring a particle's location frame by frame, MSPT also allows us to determine its respective mass in a time-resolved fashion, thus enabling the detection of attachment and detachment events along the trajectory of a single particle (Fig. 3a and Supplementary Fig. 14). For MinD, the minimal expected mass increment (33 kDa) for monomer-wise turnover was close to the measurement uncertainty (28 kDa s.d.) of the mass for a single frame. To minimize user bias, we used a step-finding algorithm that locates mass change points along trajectories based on statistical criteria[46].

Figure 3b displays examples of mass time courses for individual particles and the mass steps detected by the algorithm. Note that in most cases, MinD complexes retained their size throughout their entire trajectory (Fig. 3b, upper panel). However, in roughly 10% of trajectories, the mass of a tracked particle changed during its trajectory (Fig. 3b, bottom panel), suggesting the attachment or detachment of MinD subunits to and from the membrane-bound complex. By analyzing the sizes of mass steps along all trajectories, it was possible to obtain a distribution of subunit sizes attaching and detaching from membrane-bound MinD complexes (Fig. 3c), which appeared to mostly (dis-)assemble in one- or two-subunit increments at low particle densities. However, for higher MinD particle densities, when larger oligomers had accumulated, these complexes often turned over greater subunits, as indicated by the
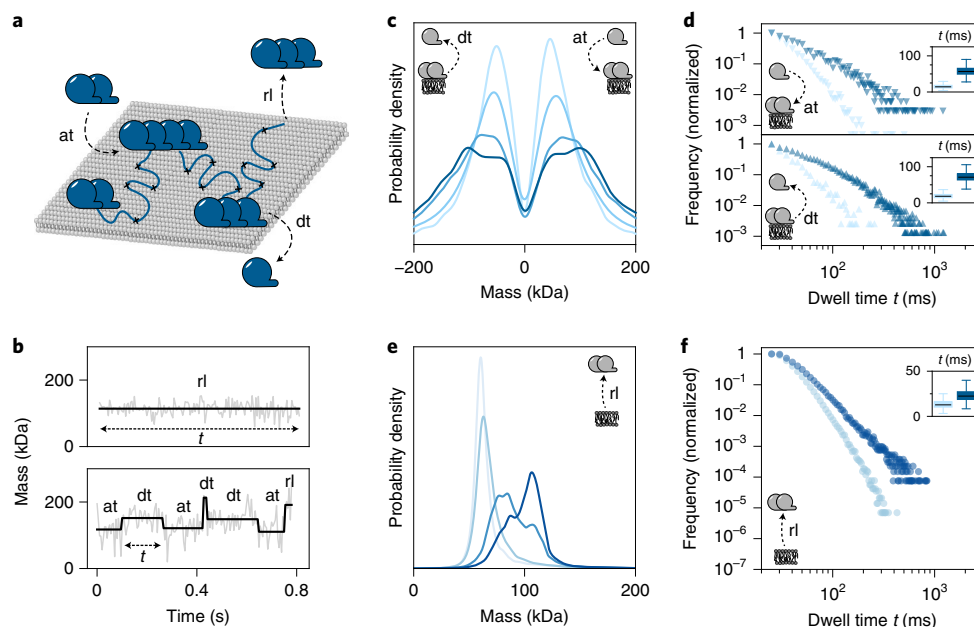
Fig. 3 | Subunit (dis-)assembly of MinD particles diffusing on membranes. a, Schematic representation of the time-resolved mass analysis of single MinD trajectories, which reveals attachment (at) and detachment (dt) events along the trajectory as well as a particle's full membrane release (rl) at the end of its trajectory. **b**, Representative mass time traces of MinD trajectories (gray line) and corresponding step fits (black line) determined by a step-finding algorithm that locates mass change points within a trajectory. **c**, Mass step size distribution derived from step fits as depicted in **b** revealing MinD subunit sizes for at and dt events at particle densities: $0.1\,\mu m^{-2}$, pale blue ($n=20,796$ plateaus); $0.3\,\mu m^{-2}$, light blue ($n=26,177$ plateaus); $0.6\,\mu m^{-2}$, blue ($n=25,864$ plateaus) and $0.8\,\mu m^{-2}$, dark blue ($n=7,506$ plateaus). **d**, Dwell time plots for MinD particles before at events (top plot), representing the lengths of mass plateaus preceding a mass increase and before dt events (bottom plot), representing the lengths of mass plateaus preceding a mass decrease. Dwell times are shown for the MinD dimer (66 kDa) (light blue triangles) and the MinD tetramer state (132 kDa) (dark blue triangles). Plateau numbers for at are dimer, $n=23,782$; tetramer, $n=5,088$ and for dt are dimer, $n=3,143$; tetramer, $n=10,406$. Inset shows box plots that indicate second and third quantile (box), median (horizontal line) and 1.5× the interquartile range (whiskers) of bootstrapped mean dwell times ($n=10,000$). **e**, MinD mass distribution for rl events. MinD particle densities: $0.1\,\mu m^{-2}$, pale blue ($n=117,086$ plateaus); $0.3\,\mu m^{-2}$, light blue ($n=169,957$ plateaus); $0.6\,\mu m^{-2}$, blue ($n=284,916$ plateaus) and $0.8\,\mu m^{-2}$, dark blue ($n=120,654$ plateaus). **f**, Plot of the dwell times before rl for the MinD dimer (light blue) and tetramer state (dark blue). Plateau numbers are dimer, $n=562,011$; tetramer, $n=73,037$. Inset shows box plots, details of which are as described in **d**.

shift of the distribution toward higher mass steps[27] (Fig. 3c, dark blue profile). Moreover, the combined information of a mass plateau level and its dwell time as annotated in Fig. 3b could be used to extract the subunit turnover rates of each oligomer species (Fig. 3d). Here, the dwell time preceding a mass increase could be used to deduce subunit attachment rates (Fig. 3d, upper panel) whereas the dwell time followed by a mass decrease provided an estimate of detachment rates (Fig. 3d, lower panel). The resulting lifetime plots suggested that membrane-attached dimers had a faster subunit turnover than tetramers, indicating a higher stability of these larger complexes.

Plateaus at the end of trajectories (Fig. 3b, bottom panel, last plateau), and trajectories without any mass change at all (Fig. 3b, top panel), could be used to identify the molecular weight of particles completely released (rl) from the membrane (Fig. 3e). Notably, this time-resolved mass analysis of the individual trajectories improved the mass resolution compared to the median-based particle mass estimates used in Fig. 2. Hence, MinD dimers, trimers and tetramers were now fully resolved as separate peaks (Fig. 3e). Accordingly, one could now recognize that the major species released from the membrane was a dimer at low particle densities and a tetramer at high particle densities. The corresponding dwell time plot showed that tetramers stayed associated to the bilayer substantially longer than dimers, in line with a higher avidity in membrane binding conferred by additional MTS (Fig. 3f). For comparison, the dimer-arrested mutant MinD D40A almost exclusively dissociated as dimers or tetramers (Supplementary Figs. 15, and 16). Taken together,

our detailed trajectory analysis confirms our previous observations suggesting that MinD WT assembles into species of higher order with an intermediate trimer state. This indicates that subunits bind at a location different from the canonical dimerization site.

MinE-induced formation of large heteromeric complexes. In the past decade, several different mechanistic models have been proposed to explain the role of the ATPase-activating protein MinE for MinDE detachment dynamics[13,47,48]. Some of these models are based on the cooperation of both MinE and MinD dimer to prompt membrane release through MinD ATPase activity stimulation[43,47]. However, this effect alone cannot explain the recently observed cooperative membrane detachment of MinDE filaments[27]. To address this issue, we used MSPT to determine the stoichiometry of the membrane-bound MinDE complex and followed its membrane dynamics on a molecular level.

In accordance with previous structural studies that suggest a conformational switch of MinE allowing MinD binding only on the encounter of membrane-bound MinD[47,49], we found no indication for MinDE interaction in solution (Supplementary Fig. 17). In the presence of a SLB, however, the MinDE complex existed predominantly in a stable double-dimeric state (Fig. 4a, light pink and Supplementary Fig. 18). Furthermore, if the MinDE complex encountered more proteins on a crowded bilayer, MinE promoted the interconnection into very large heteromeric MinDE complexes, a behavior unexpected considering the common models (Fig. 4a, magenta). One possible explanation for this behavior is
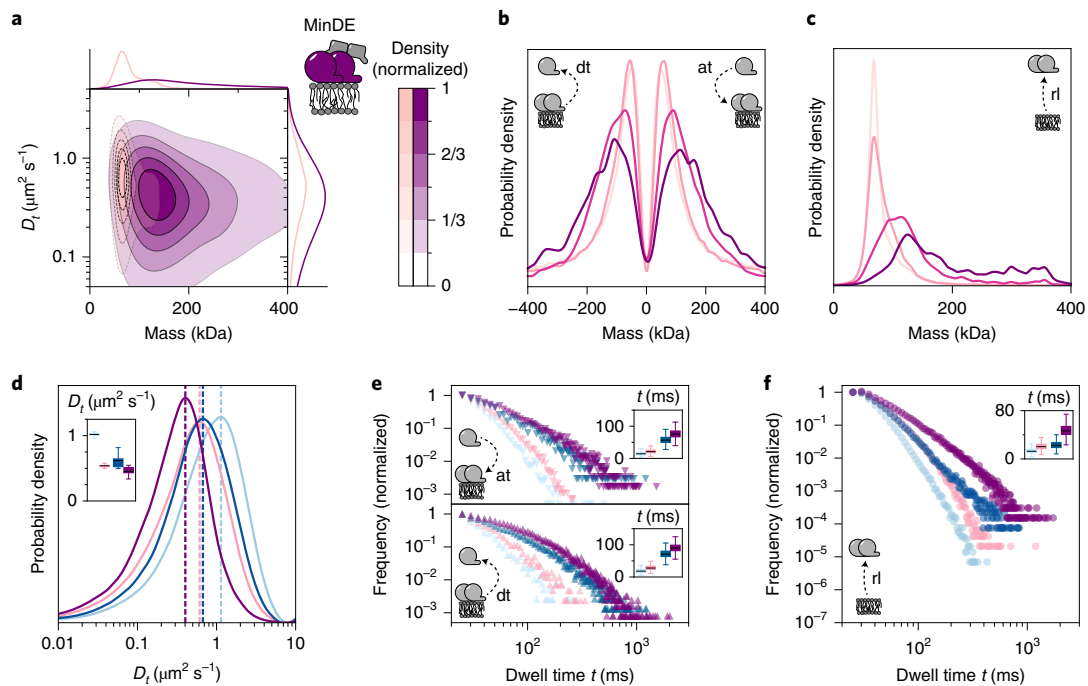
Fig. 4 | MinE interconnects MinD oligomers into large complexes with a prolonged membrane dwell time. a, Two-dimensional KDE of membrane-attached MinDE complexes at particle densities of 0.1 μm⁻² (pink) (n = 200,436 trajectories) and 0.8 μm⁻² (purple) (n = 30,082 trajectories). Marginal probability distributions of molecular mass (top) and diffusion coefficient (right) are presented. **b**, Mass step size distribution revealing MinDE subunit turnover (at and dt events) on membrane-bound particles at particle densities of 0.1 μm⁻², pale pink (n = 105,438 plateaus); 0.3 μm⁻², light pink (n = 73,471 plateaus); 0.6 μm⁻², pink (n = 9,247 plateaus) and 0.8 μm⁻², purple (n = 4,040 plateaus). **c**, MinDE mass distribution for membrane release (rl) at MinDE membrane particle densities of: 0.1 μm⁻², pale pink (n = 200,436 plateaus); 0.3 μm⁻², light pink (n = 158,660 plateaus); 0.6 μm⁻², pink (n = 35,501 plateaus) and 0.8 μm⁻², purple (n = 30,082 plateaus). **d**, Analysis of oligomer-specific diffusion coefficients for MinD (blue lines) and MinDE complexes (pink lines). Light blue/pink, dimer (MinD/MinDE n = 439,568/206,422 trajectories); dark blue/purple, tetramer (MinD/MinDE n = 118,922/47,136 trajectories). Inset shows box plots that indicate second and third quantiles (box), median (horizontal line) and 1.5× the interquartile range (whiskers) of bootstrapped diffusion coefficient maximum (n = 10,000). **e**, Dwell time plots for MinD and MinDE attachment (at) events (top) as well as for detachment (dt) events (bottom). Dwell times are shown for the MinD dimer (light blue) and tetramer (dark blue) as well as for their respective MinDE versions (hetero-dimer state, pink; hetero-tetramer state, purple). Plateau numbers for at are dimer MinD/MinDE n = 23,782/37,278; tetramer MinD/MinDE n = 5,088/11,698 and for dt are dimer MinD/MinDE n = 3,143/3,974, tetramer MinD/MinDE n = 10,406/22,501. Inset shows box plot details, as described in **d** for mean dwell times. **f**, Plot of the dwell times before rl for the MinDE dimer and tetramer state and the respective MinD versions. Plateau numbers are dimer MinD/MinDE n = 562,011/277,782; tetramer MinD/MinDE n = 73,037/60,114. Inset shows box plot details, as described in **e**.

the ability of a MinE dimer to symmetrically bind to both sides of a MinD dimer, thus effectively acting as a bridge between MinD assemblies[48]. Accordingly, our time-resolved mass step analysis revealed that during subunit turnover on membrane-bound particles, predominantly dimeric and tetrameric subunits attached and detached at high particle densities of 0.6 and 0.8 μm⁻² (Fig. 4b and Supplementary Fig. 19). This effect required a critical minimum density on the bilayer, since MinDE complexes in sparsely populated environments (0.1 and 0.3 μm⁻²) mainly exhibited conversion in their minimum subunit increments. Hence, their final oligomeric state during membrane release resembled a MinDE dimer (Fig. 4c, light pink). On bilayers with high protein density, MinDE complex sizes released from the membrane increased beyond the sizes observed for MinD alone and reached masses of >350 kDa (Fig. 4c, purple).

Based on our mass dwell time analysis, we found that the presence of MinE generally reduced the diffusion coefficients (Fig. 4d) of MinDE oligomers and slowed down turnover rates (Fig. 4e, pink), when compared to their respective MinD versions (Fig. 4e, blue). In addition, MinDE complexes were found to reside on the membrane for longer before full release (Fig. 4f). This indicates that MinE can effectively stabilize membrane-bound MinD when present in equimolar amounts as previously suggested[13,48].

Discussion

In this work, we presented a simple and versatile single-molecule-based method for the determination of membrane-associated oligomer distributions, subunit turnover and mass-resolved residence times in the context of the *E. coli* Min system. Based on our results, we propose the extension of the established membrane binding–unbinding models for MinDE self-organization[43,47] (Fig. 5). Our data support the original model regarding nucleotide exchange from ADP to ATP triggering membrane-dependent dimerization of MinD, thus coupling the process to energy dissipation. On the membrane, we find that lateral MinD interactions as well as recruitment of MinD subunits from solution lead to the formation of a dynamic mixture of MinD oligomeric states that assemble through attachment and detachment of subunits at a location different from the canonical dimerization site[31], a behavior unexpected by common models. We assume that the ability of MinD to assemble into these complexes is generally required for its local self-accumulation and in combination with the initial nucleotide-dependent membrane recruitment explains the observed attachment cooperativity during MinDE self-organization. At elevated membrane densities, a small percentage of MinD self-assembles into tetramers, which either fall apart or interact with MinE. In contrast to the previously assumed cooperation of the MinE and MinD dimer to prompt
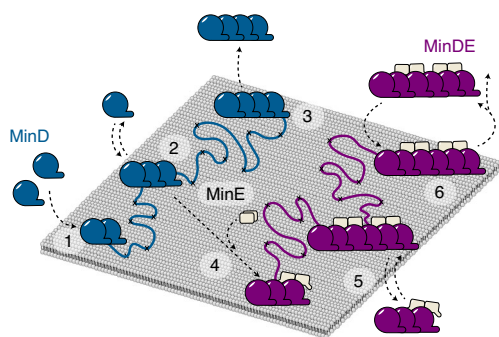
Fig. 5 | Schematic of the proposed membrane-associated MinDE reaction cycle. 1. On nucleotide exchange from ADP to ATP, membrane-dependent dimerization of MinD is triggered. 2. On the membrane, lateral MinD interactions and recruitment of MinD subunits from solution lead to MinD higher-order structures that assemble through attachment of subunits at a location different from the canonical dimerization site. MinD assemblies then either dissociate from the membrane (3) or encounter MinE (4). MinE promotes the interconnection of very large heteromeric MinDE complexes that, due to their multivalent MTS structure, reside substantially longer on the membrane interface (5). 6. However, MinE also induces nucleotide-conversion of MinD subunits, thereby weakening the overall membrane avidity of the MinDE complex, before its full release from the membrane interface in complexes >350 kDa.

membrane release[43,47], we found that MinE promotes the interconnection[48] of heteromeric MinDE complexes. We assume that this behavior is based on the ability of two MinE dimers to symmetrically bind to both sides of MinD dimers, thus effectively acting as a bridge between MinD assemblies[48]. The existence of multivalent membrane-bound structures would likewise explain the prolonged residence times of MinDE complexes compared to their respective MinD oligomer variants. Notably, opposed to the previously assumed monomer detachment[50], we found MinDE to detach from the membrane interface in complexes with sizes beyond 350 kDa, which could correspond to eight MinDE subunits. This corroborates that MinE could induce nucleotide-conversion of MinD subunits and thereby weakens the overall membrane avidity of the MinDE complex before its full dissociation from the membrane interface[27]. On membrane release, larger complexes might remain temporarily stable, stay in the vicinity of the bilayer, and can potentially rebind close to their dissociation spot, once MinD subunits have exchanged their nucleotide. An indication of such behavior is the gradual shift of MinD/MinDE mass distributions, for both membrane recruitment and release events, toward higher masses over the course of a video (Supplementary Fig. 20). To conclude, we believe that MinDE self-organization arises from an interplay of cooperative MinD membrane attachment into higher-order oligomers, anisotropy of the local MinD concentration through quick re-binding of oligomers to the membrane and ATP-dependent membrane release of MinD assemblies coordinated by the ATPase-stimulating activity of MinE.

The mechanistic dissection of the MinDE membrane cycle described in this study constitutes a detailed technical demonstration of the capabilities of MSPT. By combining the advantages of mass photometry[17,18], where biomolecular complex stoichiometries are determined from the mass of individual particles, with SPT, MSPT provides invaluable insights into the complex dynamics of biomolecules on lipid membranes. When exploring the size range for quantitative characterization of transient membrane interactions and oligomer stoichiometries, we found that >50 kDa proteins on SLBs could be reliably resolved with our system at relatively low particle densities (Supplementary Discussion). Although the

application to even smaller proteins will require improved methodology with regard to detection and data processing, the ability of label-free detection of membrane complexes provides powerful advantages over conventional fluorescence-based SPT approaches: (1) the possibility to simultaneously determine particle densities, that is local concentrations on the bilayer; (2) the correlation of mass and diffusion coefficient, which, in combination with a derived membrane inclusion size, provides information about the stoichiometry and arrangement of a membrane-bound complex; (3) the analysis of time-resolved subunit turnover and its kinetics by analyzing mass changes along a particle's trajectory and (4) extended observation times due to the absence of photobleaching, thus enabling the collection of high particle statistics in a short period of time. Ultimately, we believe that MSPT will make a strong contribution to the quantitative understanding of both prokaryotic and eukaryotic membrane-associated biological systems.

Online content

Any methods, additional references, Nature Research reporting summaries, source data, extended data, supplementary information, acknowledgements, peer review information; details of author contributions and competing interests; and statements of data and code availability are available at https://doi.org/10.1038/s41592-021-01260-x.

References

1. Gonzalez, L. & Scheller, R. H. Regulation of membrane trafficking: structural insights from a Rab/effector complex. *Cell* **96**, 755–758 (1999).
2. Cho, W. & Stahelin, R. V. Membrane-protein interactions in cell signaling and membrane trafficking. *Annu. Rev. Biophysics Biomolecular Struct.* **34**, 119–151 (2005).
3. Bagheri, Y., Ali, A. A. & You, M. Current methods for detecting cell membrane transient interactions. *Front. Chem.* **8**, 603259 (2020).
4. Miller, H., Zhou, Z., Shepherd, J., Wollman, A. J. M. & Leake, M. C. Single-molecule techniques in biophysics: a review of the progress in methods and applications. *Rep. Prog. Phys.* **81**, 024601 (2018).
5. Manzo, C. & Garcia-Parajo, M. F. A review of progress in single particle tracking: from methods to biophysical insights. *Rep. Progr. Phys.* **78**, 124601 (2015).
6. Gelles, J., Schnapp, B. J. & Sheetz, M. P. Tracking kinesin-driven movements with nanometre-scale precision. *Nature* **331**, 450–453 (1988).
7. Funatsu, T., Harada, Y., Tokunaga, M., Saito, K. & Yanagida, T. Imaging of single fluorescent molecules and individual ATP turnovers by single myosin molecules in aqueous solution. *Nature* **374**, 555–559 (1995).
8. Schmidt, T., Schütz, G. J., Baumgartner, W., Gruber, H. J. & Schindler, H. Imaging of single molecule diffusion. *Proc. Natl Acad. Sci. USA* **93**, 2926–2929 (1996).
9. Taylor, R. W. et al. Interferometric scattering microscopy reveals microsecond nanoscopic protein motion on a live cell membrane. *Nat. Photonics* **13**, 480–487 (2019).
10. Kukura, P. et al. High-speed nanoscopic tracking of the position and orientation of a single virus. *Nat. Methods* **6**, 923–927 (2009).
11. Jacobsen, V., Stoller, P., Brunner, C., Vogel, V. & Sandoghdar, V. Interferometric optical detection and tracking of very small gold nanoparticles at a water-glass interface. *Opt. Express* **14**, 405 (2006).
12. Ueno, H. et al. Simple dark-field microscopy with nanometer spatial precision and microsecond temporal resolution. *Biophys. J.* **98**, 2014–2023 (2010).
13. Loose, M., Fischer-Friedrich, E., Herold, C., Kruse, K. & Schwille, P. Min protein patterns emerge from rapid rebinding and membrane interaction of MinE. *Nat. Struct. Mol. Biol.* **18**, 577–583 (2011).
14. Ha, T. & Tinnefeld, P. Photophysics of fluorescent probes for single-molecule biophysics and super-resolution imaging. *Annu. Rev. Phys. Chem.* **63**, 595–617 (2012).
15. Garcia-Parajo, M. F., Segers-Nolten, G. M. J., Veerman, J. A., Greve, J. & Van Hulst, N. F. Real-time light-driven dynamics of the fluorescence emission in single green fluorescent protein molecules. *Proc. Natl Acad. Sci. USA* **97**, 7237–7242 (2000).
16. Lindfors, K., Kalkbrenner, T., Stoller, P. & Sandoghdar, V. Detection and spectroscopy of gold nanoparticles using supercontinuum white light confocal microscopy. *Phys. Rev. Lett.* **93**, 037401 (2004).

17. Young, G. et al. Quantitative mass imaging of single biological macromolecules. *Science* **360**, 423–427 (2018).

18. Piliarik, M. & Sandoghdar, V. Direct optical sensing of single unlabelled proteins and super-resolution imaging of their binding sites. *Nat. Commun.* **5**, 4495 (2014).

19. de Boer, P. A. J., Crossley, R. E. & Rothfield, L. I. A division inhibitor and a topological specificity factor coded for by the minicell locus determine proper placement of the division septum in E. coli. *Cell* **56**, 641–649 (1989).

20. Raskin, D. M. & de Boer, P. A. MinDE-dependent pole-to-pole oscillation of division inhibitor MinC in *Escherichia coli*. *J. Bacteriol.* **181**, 6419–6424 (1999).

21. Raskin, D. M. & De Boer, P. A. J. Rapid pole-to-pole oscillation of a protein required for directing division to the middle of *Escherichia coli*. *Proc. Natl Acad. Sci. USA* **96**, 4971–4976 (1999).

22. Szeto, T. H., Rowland, S. L., Rothfield, L. I. & King, G. F. Membrane localization of MinD is mediated by a C-terminal motif that is conserved across eubacteria, archaea, and chloroplasts. *Proc. Natl Acad. Sci. USA* **99**, 15693–15698 (2002).

23. Hu, Z., Gogol, E. P. & Lutkenhaus, J. Dynamic assembly of MinD on phospholipid vesicles regulated by ATP and MinE. *Proc. Natl Acad. Sci. USA* **99**, 6761–6766 (2002).

24. Hsieh, C. W. et al. Direct MinE-membrane interaction contributes to the proper localization of MinDE in E. coli. *Mol. Microbiol.* **75**, 499–512 (2010).

25. Shih, Y. L. et al. The N-terminal amphipathic helix of the topological specificity factor mine is associated with shaping membrane curvature. *PLoS ONE* **6**, e21425 (2011).

26. Loose, M., Fischer-Friedrich, E., Ries, J., Kruse, K. & Schwille, P. Spatial regulators for bacterial cell division self-organize into surface waves in vitro. *Science* **320**, 789–792 (2008).

27. Miyagi, A., Ramm, B., Schwille, P. & Scheuring, S. High-speed atomic force microscopy reveals the inner workings of the MinDE protein oscillator. *Nano Lett.* **18**, 288–296 (2018).

28. Ayed, S. H. et al. Dissecting the role of conformational change and membrane binding by the bacterial cell division regulator MinE in the stimulation of MinD ATPase activity. *J. Biol. Chem.* **292**, 20732–20743 (2017).

29. Ghosal, D., Trambaiolo, D., Amos, L. A. & Löwe, J. MinCD cell division proteins form alternating co-polymeric cytomotive filaments. *Nat. Commun.* **5**, 5341 (2014).

30. Ye, W. et al. Plasmonic nanosensors reveal a height dependence of MinDE protein oscillations on membrane features. *J. Am. Chem. Soc.* **140**, 51, 17901–17906 (2018).

31. Heermann, T., Ramm, B., Glaser, S. & Schwille, P. Local self-enhancement of MinD membrane binding in Min protein pattern formation. *J. Mol. Biol.* **432**, 3191–3204 (2020).

32. Kretschmer, S., Zieske, K. & Schwille, P. Large-scale modulation of reconstituted Min protein patterns and gradients by defined mutations in MinE's membrane targeting sequence. *PLoS ONE* **12**, 1–16 (2017).

33. Ortega Arroyo, J. et al. Label-free, all-optical detection, imaging, and tracking of a single protein. *Nano Lett.* **14**, 2065–2070 (2014).

34. Mosby, L. S. et al. Myosin II filament dynamics in actin networks revealed with interferometric scattering microscopy. *Biophys. J.* **118**, 1946–1957 (2020).

35. Howarth, M. et al. A monovalent streptavidin with a single femtomolar biotin binding site. *Nat. Methods* **3**, 267–273 (2006).

36. Weimann, L. et al. A quantitative comparison of single-dye tracking analysis tools using Monte Carlo simulations. *PLoS ONE* **8**, e64287 (2013).

37. Johansson, B., Höök, F., Klenerman, D. & Jönsson, P. Label-free measurements of the diffusivity of molecules in lipid membranes. *Chem. Phys. Chem.* **15**, 486–491 (2014).

38. Horton, M. R., Höfling, F., Rädler, J. O. & Franosch, T. Development of anomalous diffusion among crowding proteins. *Soft Matter* **6**, 2648–2656 (2010).

39. Horton, M. R., Reich, C., Gast, A. P., Rädler, J. O. & Nickel, B. Structure and dynamics of crystalline protein layers bound to supported lipid bilayers. *Langmuir* **23**, 6263–6269 (2007).

40. Hu, Z. & Lutkenhaus, J. Topological regulation of cell division in *E. coli*: spatiotemporal oscillation of MinD requires stimulation of its ATPase by MinE and phospholipid. *Mol. Cell* **7**, 1337–1343 (2001).

41. Ramm, B. et al. The MinDE system is a generic spatial cue for membrane protein distribution in vitro. *Nat. Commun.* **9**, 3942 (2018).

42. Wu, W., Park, K. T., Holyoak, T. & Lutkenhaus, J. Determination of the structure of the MinD-ATP complex reveals the orientation of MinD on the membrane and the relative location of the binding sites for MinE and MinC. *Mol. Microbiol.* **79**, 1515–1528 (2011).

43. Park, K. T., Wu, W., Lovell, S. & Lutkenhaus, J. Mechanism of the asymmetric activation of the MinD ATPase by MinE. *Mol. Microbiol.* **85**, 271–281 (2012).

44. Evans, E. & Sackmann, E. Translational and rotational drag coefficients for a disk moving in a liquid membrane associated with a rigid substrate. *J. Fluid Mech.* **194**, 553–561 (1988).

45. Khmelinskaia, A., Mücksch, J., Petrov, E. P., Franquelim, H. G. & Schwille, P. Control of membrane binding and diffusion of cholesteryl-modified DNA origami nanostructures by DNA spacers. *Langmuir* **34**, 14921–14931 (2018).

46. Little, M. A. et al. Steps and bumps: precision extraction of discrete states of molecular machines. *Biophys. J.* **101**, 477–485 (2011).

47. Park, K. T. et al. The min oscillator uses MinD-dependent conformational changes in MinE to spatially regulate cytokinesis. *Cell* **146**, 396–407 (2011).

48. Vecchiarelli, A. G. et al. Membrane-bound MinDE complex acts as a toggle switch that drives Min oscillation coupled to cytoplasmic depletion of MinD. *Proc. Natl Acad. Sci. USA* **113**, E1479–E1488 (2016).

49. Ghasriani, H. & Goto, N. K. Regulation of symmetric bacterial cell division by MinE What is the role of conformational dynamics? *Commun. Integr. Biol.* **4**, 101–103 (2011).

50. Lackner, L. L., Raskin, D. M. & De Boer, P. A. J. ATP-dependent interactions between *Escherichia coli* Min proteins and the phospholipid membrane in vitro. *J. Bacteriol.* **185**, 735–749 (2003).

51. Stellmacher, L. et al. Acid-base catalyst discriminates between a fructose 6-phosphate aldolase and a transaldolase. *Chem. Cat. Chem.* **7**, 3140–3151 (2015).

Methods

ADP/ATP stock solution. Both ADP and ATP stocks were prepared from their respective salt hydrates (nos. A2754 and A2383, Sigma Aldrich), supplemented with an equal molar amount of MgCl$_2$, and adjusted to pH 7.5 with 1 M Tris-HCl. Final nucleotide concentration was spectroscopically determined (wavelength $\lambda = 259$ nm; V-650, Jasco) using an extinction coefficient of 15,400 M^{-1} cm^{-1}.

Protein purification and modification. Purifications of MinD, MinD D40A and MinE were performed as previously described[52] and all used plasmid constructs are indicated in Supplementary Table 4. Divalent streptavidin was assembled as outlined in Howarth et al.[53], both pET21a-Streptavidin-Alive (Addgene plasmid no. 20860) and pET21a-Streptavidin-Dead (Addgene plasmid no. 20859) were a gift from A. Ting[35]. Biotin-modification of aldolase (no. 28403842, Cytiva) with EZ-Link Maleimide-PEG2-Biotin (no. A39261, Thermo Fisher Scientific) was achieved through incubation at room temperature for 1 h and subsequent size-exclusion chromatography on a 16/600 Superdex 200 pg column (Cytiva), equilibrated in storage buffer (50 mM HEPES pH 7.25, 150 mM KCl, 0.1 mM EDTA, 10% glycerol, 0.4 mM TCEP), using an Äkta Pure chromatography system (Cytiva). LC–MS and SDS–PAGE was performed to assess purity and integrity of all purified or modified proteins. A customized Bradford assay (no. 5000006, Bio-Rad Protein Assay; Bio-Rad Laboratories Inc.) was used to determine protein concentrations and single-use aliquots were flash frozen in liquid nitrogen and stored at −80 °C.

Small unilamellar vesicles (SUVs) and SLB formation. For the formation of SUVs, DOPC (no. 850375, Avanti Polar Lipids), dioleoyl-sn-glycero-3-phosphoglycerol (DOPG) (no. 840475, Avanti Polar Lipids) and 1,2-dioleoyl-sn-glycero-3-phosphoethanolamine-N-cap biotinyl (18:1 Biotinyl Cap PE; no. 870273, Avanti Polar Lipids) were dissolved in chloroform (Sigma Aldrich) and mixed in a ratio of 70 mol% DOPC to 30 mol% DOPG or 70 mol% DOPC with 29.99 mol% DOPG and 0.01 mol% Biotinyl Cap PE. After solvent evaporation through nitrogen, residual chloroform was removed for 1 h in a vacuum desiccator. Lipid film hydration was achieved with Min buffer (25 mM Tris/HCl pH 7.5, 150 mM KCl, 5 mM MgCl$_2$) and SUVs were formed through consecutive freeze–thaw cycles (8–10) using liquid nitrogen and a 90 °C water bath. For monodisperse vesicle distribution, lipid mixtures were extruded across a Whatman nucleopore membrane (no. 110603, Cytiva) with a pore size of 50 nm for 37 passes.

SLBs were formed by fusion of SUVs on cleaned glass cover slides (Paul Marienfeld GmbH & Co. KG) that were assembled into a flow chamber through double-sided sticky tape (Scotch, Conrad Electronic SE). Before their assembly, cover slides (nos. 0102242, 1.5, 24 × 60 mm²; nos. 0102062, 1.5, 24 × 24 mm²) were cleaned by sequential sonication in Milli-Q water, isopropanol and Milli-Q water (15 min each), and subsequently dried under a nitrogen stream. Slides were then activated for 30 s (30% power, 0.3 mbar) in a Zepto plasma cleaner (Diener Electronic GmbH) using oxygen as the process gas. After flow chamber assembly, SUVs were added to each reaction chamber at a final concentration of 0.4 mg ml^{-1} in Min buffer with additional 2 mM CaCl$_2$ to promote vesicle rupture. Unfused SUVs were removed through subsequent washing with Min buffer.

Mass calibration curves and diffusion control. To convert interferometric scattering contrast into the respective protein mass, the contrast of a set of mass standards was measured for each experimental setup: mass photometry landing assays and MSPT on the lipid interface. In line with Young et al.[17], mass calibration for landing assays was performed in flow chambers filled with filtered (sterile syringe filters with a 0.45 µm cellulose acetate membrane, VWR International) SLB buffer (25 mM Tris/HCl pH 7.5, 150 mM KCl). As mass standards, 50 nM tobacco etch virus (TEV) protease (MPIB Core Facility), 50 nM Pierce recombinant protein A (no. 21184, Thermo Fisher Scientific) 50 nM bovine serum albumin (BSA) (no. A4612, Sigma Aldrich), 20 nM alcohol dehydrogenase (no. A8656, Sigma Aldrich) or 20 nM β-amylase (no. A8781, Sigma Aldrich) were injected and landing events recorded. To also enable mass calibration on SLBs, membranes containing 0.01 mol% Biotinyl Cap PE were used. As linker for the attachment of biotinylated standard proteins, 2.5 nM divalent streptavidin were incubated for 10 min (room temperature) before the addition of 100 nM biotin labeled bovine albumin (no. A8549, Sigma Aldrich), biotinylated Pierce protein A (no. 29989, Thermo Fisher Scientific) or custom biotinylated aldolase (no. 28403842, Cytiva). These concentrations corresponded to 3–6 particles (median value) in the FOV for each standard protein, equivalent to a particle density of 0.09 to 0.19 µm^{-2}.

For diffusion coefficient verification, 1.25 nM unconjugated tetravalent streptavidin (no. SNN1001, Thermo Fisher Scientific) were incubated for 10 min (room temperature) on a supported lipid membrane containing biotinylated lipids.

Mass photometry landing assay. To determine the nucleotide-dependent solution-state of MinD (175 nM) and MinDE (175 nM), all proteins were diluted in filtered (sterile syringe filters, 0.45 µm cellulose acetate membrane, VWR International) Min buffer in the presence of either 0.5 mM ADP or ATP. Measurements were performed in flow chambers and 50 µl of protein solution were flushed in five times consecutively to collect sufficient landing events.

In vitro reconstitution of Min complexes on a lipid bilayer. *MinD.* For MSPT of single MinD complexes on the lipid interface, we added increasing protein concentrations (50, 75, 100, 125, 150, 175 and 200 nM, $n = 3$ flow chambers each) to a flow chamber with a SLB in the presence of 0.5 mM ATP in filtered Min buffer. The same experiments were performed likewise for MinD D40A. Videos of 0.5 mM ATP in Min buffer without protein were recorded as image background control (0.8% of particles detected as compared to videos containing MinD).

MinDE. Co-reconstitution of MinDE was performed in a similar manner to MinD, except for the addition of equimolar amounts of both reactants (50, 75, 100, 125, 150, 175 and 200 nM, $n = 3$ flow chambers each) to the sample chamber. For MinD D40AE, experiments were performed with 200 nM of each protein.

Microscopy. Imaging of MinDE landing assays was performed on a custom-built interferometric scattering microscope described in refs. [17,54] with a 445-nm laser diode for illumination and 635 nm for focus stabilization. Image acquisition was controlled using custom-written software in Labview described in ref. [17]. Landing events were recorded at a frame rate of 1 kHz for 60 s per video. Videos were saved fivefold frame-averaged (200 Hz effective frame rate) and threefold pixel binned (70.2 nm effective pixel size).

SLB experiments were carried out on a commercial Refeyn One^{MP} mass photometer (Refeyn Ltd). Videos were acquired for either 45 s (landing assay of mass standards, Fig. 1) or 350 s (SLB assays) with the AquireMP (Refeyn Ltd, v.2.3) software at a frame rate of 1 kHz. Videos were saved fivefold frame-averaged (200 Hz effective frame rate) and fourfold pixel-binned (84.4 nm effective pixel size). Measurements were performed at room temperature (23 ± 2 °C).

Data analysis. *Image processing of conventional mass photometry landing assays.* Videos of the proteins MinD, MinE and their equimolar mixture MinDE landing on glass cover slides were analyzed with the software DiscoverMP (v.2.1.0, Refeyn Ltd), using a rolling background removal strategy[17].

MinD monomers have a molecular mass of 33 kDa, which approaches the lower detection limit of the mass photometer. We have therefore systematically determined the optimal frame averaging factor navg and filter thresholds T1 and T2 for the detection of MinD monomers and dimers. To this end, we generated a semisynthetic video that used frames from a video recorded in a chamber with Min buffer alone to reconstruct the experimental background and added simulated PSFs (same as fitting model PSF) as landing events that had the expected scattering contrast of MinD monomers (contrast of 1.9×10^{-3}) or MinD dimers (contrast of 3.5×10^{-3}). We then varied navg as well as T1 and T2, ran the analysis procedure and evaluated the number of true positive and false positive detections. To determine the maximum number of true positive detections possible at the respective signal-to-noise ratio, we simulated 1,000 frames with 100 landing events that were not allowed to spatially overlap closer than 12 pixels and 26 frames temporally. Based on the simulation, we chose navg = 12, T1 = 1.1 and T2 = 0.2 to process the experimental videos. Using these parameters, the number of true positive detections of monomers was 68.8 ± 6.6% (mean ± s.d., $n = 5$ simulated videos), while the total of false positive detections was 9.4 ± 2.1%. For dimers, a simulation with the same parameters gave 95.8 ± 0.8% true positive detections and 4.2 ± 1.1% false positive ones.

Mass calibration for landing assays. Landing events imaged in three independent experiments per standard protein were pooled and kernel density estimations (KDEs) were calculated. For each standard protein, the contrast associated with a probability density maximum was determined and plotted against its nominal mass (Supplementary Table 2). In case of alcohol dehydrogenase and β-amylase, the peak with higher contrast was used.

Error bars in Fig. 1c represent the standard error of the peak position calculated from 10,000 bootstrap resamples.

Image processing and analysis procedure for SPT and mass determination of biomolecules on SLBs. To detect and analyze diffusing biomolecules on a lipid bilayer, we applied a new image processing strategy that removed the dominant static scattering background, while conserving the shape of mobile features and displaying them on top of a shot noise-limited background. Around each frame, a pixel-wise temporal median image was calculated that only contains the features that did not move in the median period. This static background, calculated for each frame, was then removed from the respective frame with index i according to equation (1) and with n denoting the median half-size.

$$\text{mobile features frame}_i = \left(\frac{\text{frame}_i}{\text{median}\left(\text{frame}_{i-n} : \text{frame}_{i+n}\right)} \right) - 1 \qquad (1)$$

Through this process, moving objects in the mobile features frame appeared as undistorted PSFs and displayed iSCAT contrasts similar to those obtained for molecules in the conventional landing assay. We received a custom-written Python script from P. Kukura and G. Young (University of Oxford) that automatized this image analysis procedure and we modified it to load and process videos in the Refeyn format (.mp files). To track individual proteins diffusing on SLBs in the

background-corrected videos, the Python script also included a SPT routine. For particle detection, a Laplace filter was applied to each frame (scipy.ndimage.filters. gaussian_laplace function) to suppress shot noise and highlight potential particles. The Laplace-filtered images were thresholded, such that only objects with at least the size of 53 kDa remained, a threshold that would preserve streptavidin as our smallest standard protein and MinD dimers. Local maxima were then found (scipy. ndimage.filters.maximum_filter function) as candidate pixels that contained a particle. Around each of these candidate pixels in the non-Laplace-filtered image, a region of interest of 13×13 pixels (84.4 nm per pixel) was excised and fitted by the model PSF used in the DiscoverMP software to extract particle contrast and location at subpixel resolution. Particle locations were linked into trajectories using the Trackpy package (v.0.4.2, link_df function)[55]. Only trajectories of particles with a lifetime of at least five frames (25 ms) were considered for subsequent analyses. Supplementary Table 1 summarizes all parameters used for particle detection, fitting and trajectory linking.

Determination of diffusion coefficients. To determine translational diffusion coefficients from individual trajectories, we carried out a jump-distance analysis as described in ref. [36]. Cumulative frequency distributions of jump distances for time lags from $\Delta 1$ to $\Delta 4$ frames were fitted globally (scipy.optimize.least_squares, Trust Region Reflective algorithm) with either one or two species depending on which model resulted in a reduced chi-squared statistic.

$$P_{1c}\left(r^2, \ \Delta t\right) = 1 - e^{-\frac{r^2}{4D_1\Delta t + \sigma}} \tag{2}$$

$$P_{2c}\left(r^2, \ \Delta t\right) = 1 - \sum_{i=1}^{2} a_i \ e^{-\frac{r^2}{4D_i\Delta t + \sigma}}, \ \sum_{i=1}^{2} a_i = 1 \tag{3}$$

D_i and a_i are the diffusion coefficient and abundance of component i, Δt is the time lag and σ is an offset parameter taking into account localization uncertainty and motion blur[56]. In the case of a two-component model (around 10% of all trajectories), an effective diffusion coefficient was calculated according to

$$D_t = a_1 D_1 + a_2 D_2, \tag{4}$$

For comparison with the jump-distance approach in the diffusion simulation (Supplementary Fig. 2), diffusion coefficients were also estimated based on the mean squared displacement. Here, the first three or four nontrivial time-averaged mean squared displacement points were included in the linear regression depending on the trajectory length[56].

In both fit routines, the diffusion coefficient was restricted to values greater than $0.0001 \, \mu m^2 s^{-1}$ while the offset parameter σ was unconstrained. Trajectories where the diffusion coefficient returned by the fit hit the lower boundary were excluded from the analysis.

KDE in one dimension. For univariate distributions, KDEs were computed with the Python package KDEpy (v.1.0.10, FFTKDE function, https://github.com/ tommyod/KDEpy), using a Gaussian kernel and the Improved Sheather–Jones plug-in bandwidth selector[57].

KDE in two dimensions. Two-dimensional (2D) maps of the diffusion coefficient and mass were computed with the Python package fastkde (v.1.0.14, fastkde.pdf function)[58]. The probability density for the diffusion coefficient was calculated in base 10 logarithmic space. Marginal distributions displayed on top and on the right of the graph were calculated by summing up the bivariate probability densities along the y and x axes, respectively.

The resulting 2D kernel densities were plotted as filled contours with either six (if an overlay of two conditions is shown) or eight linearly spaced levels. The opacity of the levels was reduced linearly from 100% for the highest to 0% for the lowest level, rendering the lowest level fully transparent.

Mass calibration for MSPT. Analogous to the mass calibration for landing assays, peak contrasts were related to the nominal mass of streptavidin (Strep) or to the mass of streptavidin and the standard protein (Strep-ALD, Strep-BSA, Strep-prA). For the streptavidin–protein complexes, the peak with lowest contrast was excluded from analysis as it resembles streptavidin without an attached standard protein (blue crosses, Supplementary Fig. 4). The two other peak(s) with higher contrast were assigned to dimeric and tetrameric aldolase, monomeric and dimeric BSA and monomeric protein A (Supplementary Table 3).

Error bars in Fig. 1c represent the standard error of the peak position calculated from 10,000 bootstrap resamples.

Simulated videos of diffusing particles. To investigate the influence of extreme diffusion coefficients and high particle densities on the fidelity of our MSPT analysis, we implemented a Python routine that adds artificial diffusing particles to an experimental video of an empty SLB. Thereby, it was possible to control the number of particles in the FOV and to individually set both the iSCAT contrast and the particles' diffusion coefficients. In a first step, the trajectories of all

particles were generated by choosing a random starting location within an area that is four times the video FOV size (x and y axes extended twofold). The traveled per-frame distance Δs in the x and y directions was drawn randomly from normal distributions with standard deviation $2D\Delta t$ (equation (5)).

$$p\left(\Delta s\right) = \frac{1}{\sqrt{2\pi\left(2D\Delta t\right)^2}} e^{-\frac{s^2}{2\times\left(2D\Delta t\right)^2}} \tag{5}$$

where D is the diffusion coefficient converted into pixel dimensions and Δt the frame time. To keep the number of particles in the simulated area constant, we added periodic boundaries. Whenever a particle would cross a boundary of the simulated area, its location was shifted to the corresponding location at the opposite boundary. Trajectory coordinates that entered the FOV of the experimental video, that is, 128×35 pixels, were populated with PSFs of a defined ratiometric contrast according to the Refeyn fitting model. Finally, the background-free ratiometric video of simulated PSFs was merged with a raw experimental iSCAT video of an empty SLB via pixel-wise calculation of

$$\text{camera count}_{\text{simulated}} = (\text{contrast}_{\text{ratiometric}} + 1) \times \text{camera count}_{\text{experimental}} \tag{6}$$

The resulting simulated videos were then analyzed by our MSPT analysis routine in the same way as an experimental video with real particles.

Analysis of MinD and MinD40A oligomerization. Each trajectory was assigned to an apparent membrane protein density determined as the median of all trajectories detected during the trajectory's lifetime, divided by the area of the FOV ($31.9 \, \mu m^2$). For trajectory densities ranging from 0.03 to $0.8 \, \mu m^{-2}$ (corresponding to 1 to 27 particles in the FOV), the KDE of each mass distribution was calculated. The densities were binned in an overlapping manner, such that all trajectories were selected that had trajectory numbers within a range of plus or minus two (for example, at a density of $0.1 \, \mu m^{-2}$, corresponding to four trajectories per FOV, trajectories with membrane coverage between two and six trajectories per FOV were pooled). Each KDE was fit with a linear combination of monomer to hexamer mass distributions that were inferred from single component simulations of MinD or MinD D40A at varying particle densities (Supplementary Fig. 9). The mass distributions for each oligomer and density were selected based on the number of localized particles in the experiment as a certain fraction of particles (roughly 40%) is lost in the trajectory linking and filtering (minimum length of five frames) process (Supplementary Fig. 12). Additionally, the sum of contributions of the six components was constrained to add up to unity in the least-squares sense. Before fitting, the simulated mass distributions were smoothed using a moving average with a window length of 2.5 kDa. To estimate the uncertainty of the extracted abundances of the components, the dataset at each trajectory density was split randomly into three samples before fitting each subset individually. This procedure was repeated ten times and the average standard deviation of the per-split results was calculated.

Unless otherwise stated, the reported particle densities throughout the paper correspond to trajectory densities (that is, linked particle densities) as a more robust means to estimate the current membrane coverage (in contrast to localized particle densities; Supplementary Figs. 7 and 12).

Step detection. To detect mass change points during trajectories, we used a MATLAB (R2020a, The MathWorks) implementation of the Kalafut–Visscher algorithm[59] described in ref. [46]. While the algorithm has no parameters except the time series itself, we noticed that the results depended on the length of the time series and the position of potential change points if they were located close to the beginning or end of a trajectory. Thus, change points were more likely to be inserted, the shorter a time series was and the closer a point was to the boundaries of the time series. To address this ambiguity, we concatenated the trajectories of a specific imaging condition (for example, all videos containing MinD, Supplementary Fig. 14a) and divided this concatenated series into n subsets of equal length l, which were then analyzed with the step detection algorithm (Supplementary Fig. 14b). This procedure enabled an equal treatment of trajectories of different lengths and avoided bias in change point detection at the beginning and the end of trajectories. Additionally, step identification was repeated $l - 1$ times shifting the start point of the linked time series circularly by one increment in each iteration. This second procedure ensured that the detected steps would not depend on the start points of a subset. From the l outputs generated in total, the relative significance of a step was reflected by the fraction f of iterations, in which a change point was found at a particular location, ranging from 0 (never) to 1 (in every iteration, Supplementary Fig. 14c).

The choice of fraction f as well as the length l is arbitrary yet interconnected. Increasing l leads to fewer detected steps, which can be compensated for by reducing f. Since the longest trajectory in all datasets has a length of 558 frames and an increasing length leads to a finer grating of the tunable parameter f, we set l to 1,000 frames. By visual inspection, we chose a fraction f of 0.25 as an appropriate tradeoff between under- and over-identification of steps considering the noise level in our trajectories (Supplementary Fig. 14d).

Subunit attachment/detachment during membrane diffusion and release of complexes. The concatenated mass traces and step-fitting results were split into their original trajectories (Supplementary Fig. 14e). For each trajectory, step heights (equivalent to mass changes) and dwell lengths (equivalent to time intervals without a change of mass) were extracted and categorized into three classes (Fig. 3b). Depending on whether the sign of the succeeding mass change is positive or negative, the preceding level is classified as an attachment or as a detachment plateau, respectively. The last plateau in a trajectory before the dissociation of the whole particle from the membrane is regarded separately as release. If no step is detected in the mass time series as it was the case in roughly 90% of all trajectories, the single plateau is also classified as release. Particles leaving the FOV have been excluded from the analysis. Therefore, it can be assumed that the end of a trajectory represents the particle's release from the membrane. Generally, the mass that initially binds to the membrane is not included in the list of steps for attachment or detachment events.

The distribution of mass changes during the trajectory as well as the distribution of complex mass released from the membrane for different densities are displayed as univariate kernel density estimates. To characterize the residence times of different oligomers, histograms of the observed dwell lengths were generated for plateaus with masses that correspond to dimeric (66 ± 17 kDa) or tetrameric (132 ± 17 kDa) MinD complexes. For each variant, the average dwell times were calculated according to equation (7)

$$\bar{t} = \frac{\sum_{i=m}^{n} N_i t_i}{\sum_{i=m}^{n} N_i} - t_m, \quad (7)$$

where N_i is the total number of plateaus with dwell time t_i, and t_m represents the most frequent dwell time (m and n designate the plateaus with the most and least frequent dwell time, respectively). Due to the noise level of mass detections in our trajectories, short dwell times could not be quantitatively detected. Hence, dwell times shorter than five frames (25 ms) were excluded from the analysis.

The standard error of the mean dwell time was estimated from 10,000 bootstrap resamples.

Reporting Summary. Further information on research design is available in the Nature Research Reporting Summary linked to this article.

Data availability
Microscopy raw data and tables of detected and linked particles have been deposited in the Max Planck data service Edmond under the following https://doi.org/10.17617/3.74. Source data are provided with this paper.

Code availability
The custom-written Python script for particle detection and particle simulation (both as binary executable) as well as particle analysis (source code accessible) is available from the corresponding authors on reasonable request.

References
52. Ramm, B., Glock, P. & Schwille, P. In vitro reconstitution of self-organizing protein patterns on supported lipid bilayers. *J. Vis. Exp.* https://doi.org/10.3791/58139 (2018).
53. Howarth, M. & Ting, A. Monovalent streptavidin expression and purification. Preprint at https://doi.org/10.1038/nprot.2008.81 (2008).
54. Cole, D., Young, G., Weigel, A., Sebesta, A. & Kukura, P. Label-free single-molecule imaging with numerical-aperture-shaped interferometric scattering microscopy. *ACS Photonics* **4**, 211–216 (2017).
55. Allan, D. et al. soft-matter/trackpy: Trackpy v.0.4.2, https://doi.org/10.5281/ZENODO.3492186 (Zenodo, 2019).
56. Michalet, X. Mean square displacement analysis of single-particle trajectories with localization error: Brownian motion in an isotropic medium. *Phys. Rev. E.—Stat. Nonlinear, Soft Matter Phys.* **82**, 041914 (2010).
57. Botev, Z. I., Grotowski, J. F. & Kroese, D. P. Kernel density estimation via diffusion. *Ann. Stat.* **38**, 2916–2957 (2010).
58. O'Brien, T. A., Kashinath, K., Cavanaugh, N. R., Collins, W. D. & O'Brien, J. P. A fast and objective multidimensional kernel density estimation method: FastKDE. *Comput. Stat. Data Anal.* **101**, 148–160 (2016).
59. Kalafut, B. & Visscher, K. An objective, model-independent method for detection of non-uniform steps in noisy signals. *Comput. Phys. Commun.* **179**, 716–723 (2008).

Author contributions
T.H., F.S. and N.H. contributed equally to this work. T.H., N.H., F.S. and P.S. conceived the study. T.H. designed and performed all experiments. T.H. and B.R. designed and purified proteins. F.S. and N.H. analyzed the data. T.H., F.S. and N.H. wrote the manuscript draft. All authors discussed and interpreted results. All authors revised, reviewed and approved the paper.

Competing interests
The authors declare no competing interests.

Additional information
Supplementary information The online version contains supplementary material available at https://doi.org/10.1038/s41592-021-01260-x.

Correspondence and requests for materials should be addressed to Nikolas Hundt or Petra Schwille.

Peer review information Nature Methods thanks Jörg Enderlein, Marek Piliarik and the other, anonymous, reviewer(s) for their contribution to the peer review of this work. Rita Strack was the primary editor on this article and managed its editorial process and peer review in collaboration with the rest of the editorial team.

Reprints and permissions information is available at www.nature.com/reprints.

Corresponding author(s):   Prof. Petra Schwille
                            Dr. Nikolas Hundt

Last updated by author(s): Jul 21, 2021

Reporting Summary

Nature Research wishes to improve the reproducibility of the work that we publish. This form provides structure for consistency and transparency in reporting. For further information on Nature Research policies, see our Editorial Policies and the Editorial Policy Checklist.

Statistics

For all statistical analyses, confirm that the following items are present in the figure legend, table legend, main text, or Methods section.

n/a	Confirmed	
☐	☒	The exact sample size (*n*) for each experimental group/condition, given as a discrete number and unit of measurement
☐	☒	A statement on whether measurements were taken from distinct samples or whether the same sample was measured repeatedly
☒	☐	The statistical test(s) used AND whether they are one- or two-sided *Only common tests should be described solely by name; describe more complex techniques in the Methods section.*
☒	☐	A description of all covariates tested
☐	☒	A description of any assumptions or corrections, such as tests of normality and adjustment for multiple comparisons
☐	☒	A full description of the statistical parameters including central tendency (e.g. means) or other basic estimates (e.g. regression coefficient) AND variation (e.g. standard deviation) or associated estimates of uncertainty (e.g. confidence intervals)
☒	☐	For null hypothesis testing, the test statistic (e.g. *F*, *t*, *r*) with confidence intervals, effect sizes, degrees of freedom and *P* value noted *Give P values as exact values whenever suitable.*
☒	☐	For Bayesian analysis, information on the choice of priors and Markov chain Monte Carlo settings
☒	☐	For hierarchical and complex designs, identification of the appropriate level for tests and full reporting of outcomes
☒	☐	Estimates of effect sizes (e.g. Cohen's *d*, Pearson's *r*), indicating how they were calculated

Our web collection on statistics for biologists contains articles on many of the points above.

Software and code

Policy information about availability of computer code

Data collection	AquireMP (Refeyn Ltd., v2.3)
Data analysis	DiscoverMP (version 2.1.0, Refeyn Ltd.); Python version 3.8.5 - 1D kernel-density estimation with KDEpy (version 1.0.10) and 2D with fastkde (version 1.0.14); MATLAB R2020a Update 6; Kalafut-Visscher algorithm kvsteps function implemented by Max A. Little (http://www.maxlittle.net/software/steps_bumps_toolkit.zip)

For manuscripts utilizing custom algorithms or software that are central to the research but not yet described in published literature, software must be made available to editors and reviewers. We strongly encourage code deposition in a community repository (e.g. GitHub). See the Nature Research guidelines for submitting code & software for further information.

Data

Policy information about availability of data

All manuscripts must include a data availability statement. This statement should provide the following information, where applicable:
- Accession codes, unique identifiers, or web links for publicly available datasets
- A list of figures that have associated raw data
- A description of any restrictions on data availability

Microscopy raw data and tables of detected and linked particles have been deposited in the Max Planck data service Edmond under the following DOI: https://dx.doi.org/10.17617/3.74.

Field-specific reporting

Please select the one below that is the best fit for your research. If you are not sure, read the appropriate sections before making your selection.

☒ Life sciences ☐ Behavioural & social sciences ☐ Ecological, evolutionary & environmental sciences

For a reference copy of the document with all sections, see nature.com/documents/nr-reporting-summary-flat.pdf

Life sciences study design

All studies must disclose on these points even when the disclosure is negative.

Sample size	Sample size can be either defined as single particle/trajectory numbers or number of independent repeats of the same experiment. Particle numbers were very high for individual experiments and provided statistics to clearly determine molecule population behaviour. To show that this population behaviour was reproducible, 3 independent repeats of each experiment were considered sufficient, since deviations between repeats were low.
Data exclusions	No data was excluded.
Replication	Three independent experiments for all measurements. All replicates were used since none deviated significantly.
Randomization	Not applicable. No clinical trials involved. Single molecules provide intrinsically randomised data because their properties are unknown prior to their analysis and no data was excluded.
Blinding	Blinding was not required, since no data was excluded and the analysis routines were completely automated. Hence, analysis was intrinsically without user-bias.

Reporting for specific materials, systems and methods

We require information from authors about some types of materials, experimental systems and methods used in many studies. Here, indicate whether each material, system or method listed is relevant to your study. If you are not sure if a list item applies to your research, read the appropriate section before selecting a response.

Materials & experimental systems

n/a	Involved in the study
☒	☐ Antibodies
☒	☐ Eukaryotic cell lines
☒	☐ Palaeontology and archaeology
☒	☐ Animals and other organisms
☒	☐ Human research participants
☒	☐ Clinical data
☒	☐ Dual use research of concern

Methods

n/a	Involved in the study
☒	☐ ChIP-seq
☒	☐ Flow cytometry
☒	☐ MRI-based neuroimaging